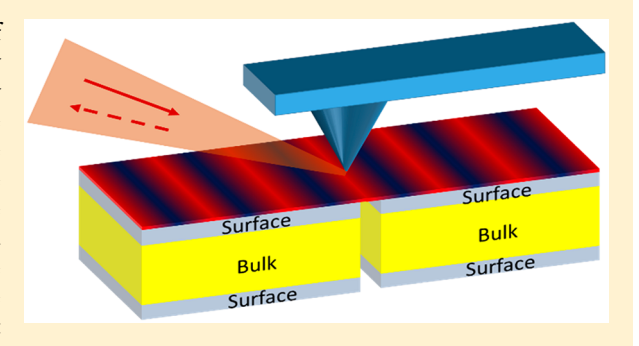


Near-Field Imaging of Surface Plasmons from the Bulk and Surface State of Topological Insulator Bi₂Te₂Se

Prabhu K. Venuthurumilli, †,‡ Xiaolei Wen,§ Vasudevan Iyer,†,‡ Yong P. Chen,‡,||,⊥,∇ and Xianfan Xu*,†,‡,⊥

Supporting Information

ABSTRACT: Surface plasmons are collective oscillations of electrons that can enable confinement of electromagnetic energy to subwavelength scales. Recent progress in plasmonics has largely relied on noble metals which are not CMOS compatible. Hence there is a need to search for new plasmonic materials. Here we show that the topological insulator Bi₂Te₂Se is plasmonic, and we study the distinct surface plasmons arising from its bulk and surface state. We launch propagating plasmon via a nanoscale slit and detect it using near-field scanning optical microscopy. We observe that the wavelength of plasmon that originated from the surface state is very short, more than 100 times smaller than the incident light wavelength, in sharp contrast to the plasmon wavelength of the



bulk which is on the order of the incident light wavelength. This short plasmon wavelength is due to the two-dimensional nature of the surface state, similar to that in graphene. The strong optical confinement of the surface state plasmons can be exploited for various applications including integrated optical circuits and subwavelength optical devices.

KEYWORDS: Bismuth telluride selenide, surface plasmon, topological insulator, bulk, surface state, near-field scanning optical microscopy

urface plasmon polaritons are electromagnetic oscillations at the interface of a dielectric and a conducting medium. Plasmons can localize the electromagnetic energy to nanoscale, well below the wavelength of light in free space. Plasmonics has emerged as a promising area in various fields such as waveguides, 1,2 biological sensing, 3-5 photovoltaics, 6 and photodetection.^{7,8} However, materials that can support surface plasmons are limited, most notably noble metals such as gold and silver. However, noble metals which are commonly used in plasmonic devices are not CMOS compatible, limiting the scaling of these devices. Hence there is a search for plasmonic materials beyond noble metals. The materials that are currently being investigated include highly doped semiconductors, transparent conducting oxides, metallic alloys, and more recently graphene and topological insulators.

Topological insulator is a family of materials with insulating bulk but has conducting electronic surface states (SS). These SS are Dirac-like and protected from backscattering 13,14 which can lead to exotic plasmonic phenomena. Recent works on the studies of topological insulators include plasmonic resonance

of Bi₂Se₃ gratings at terahertz frequencies¹⁵ and Bi_{1.5}Sb_{0.5}Te_{1.8}Se_{1.2} (BSTS) nanostructures at ultraviolet and visible frequencies.¹² In addition to these spectroscopic studies of nanostructures, real space imaging of localized plasmons was carried out using TEM-EELS on Bi₂Te₃ nanoplates¹⁶ and nearfield scanning optical microscopy (NSOM) on BSTS flakes¹⁷ and Bi₂Te₃ flakes. 18 Among the topological insulators, Bi₂Te₂Se (BTS) has been shown to have prominent SS properties and better insulation of the bulk, as its Fermi level is situated near the middle of the band gap. 19,20 In this work, we study the distinct surface plasmons arising from the bulk and SS of BTS. We launch and detect propagating surface plasmons from a nanoscale slit in BTS using NSOM and observe distinct patterns of the surface plasmons at two different incident wavelengths of 633 nm and 10.6 μ m. We attribute this to the surface plasmons from the bulk and the SS

Received: June 5, 2019 Published: September 9, 2019

[†]School of Mechanical Engineering, Purdue University, West Lafayette, Indiana 47907, United States

[‡]Birck Nanotechnology Center, Purdue University, West Lafayette, Indiana 47907, United States

[§]Center for Micro- and Nanoscale Research and Fabrication, Hefei National Laboratory for Physical Sciences at the Microscale, University of Science and Technology of China, Hefei, Anhui 230026, People's Republic of China

 $^{^{\}parallel}$ Department of Physics and Astronomy, Purdue University, West Lafayette, Indiana 47907, United States

^LSchool of Electrical and Computer Engineering, Purdue University, West Lafayette, Indiana 47907, United States

 $^{{}^{}m V}$ Purdue Quantum Center, Purdue University, West Lafayette, Indiana 47907, United States

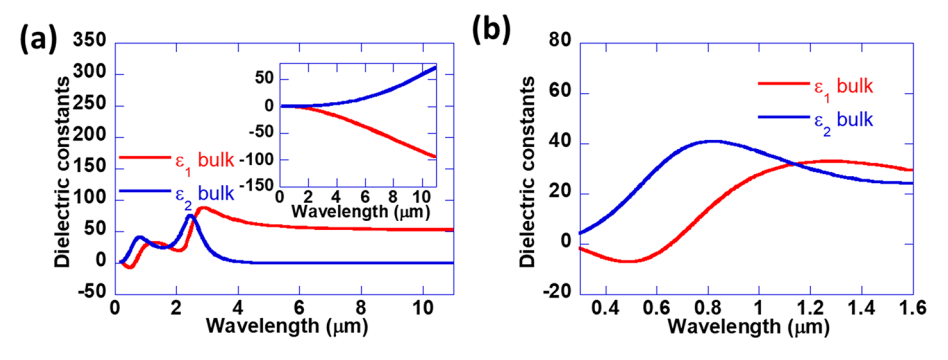


Figure 1. Dielectric constants of BTS. (a) Bulk BTS. The inset shows the dielectric constants of the surface layer and (b) enlarged view of the bulk BTS properties in the visible and near IR region.

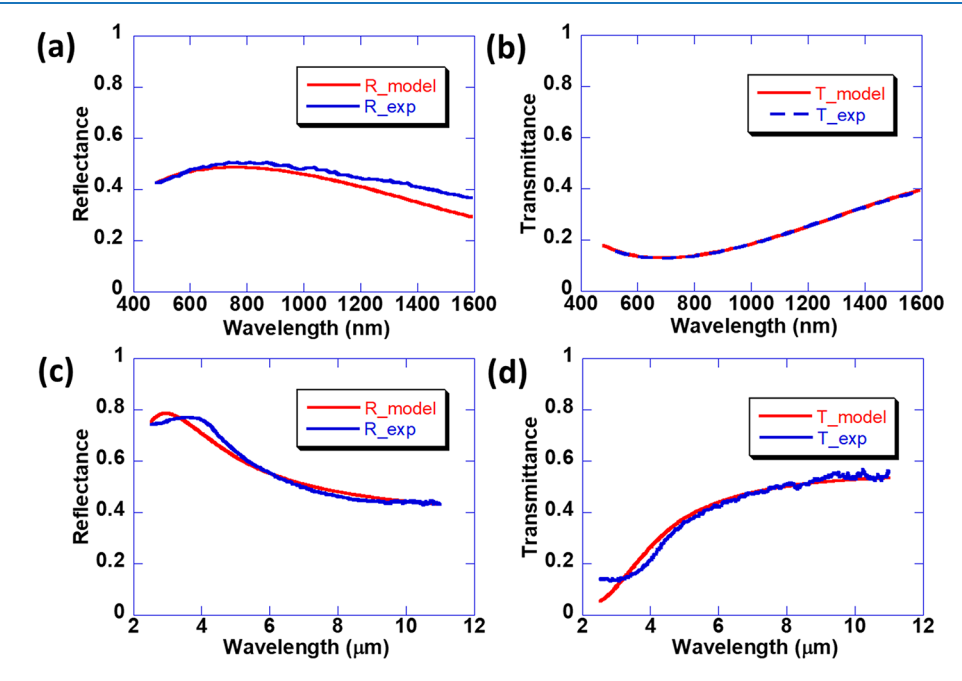


Figure 2. Optical measurements of BTS flake. (a,b) Reflectance and transmittance of 15 nm BTS flake on CaF_2 substrate and (c,d) Reflectance and transmittance of 55 nm BTS flake on undoped Si substrate. R_exp and T_exp are the experimental reflectance and transmittance, respectively. R_model and T_model are the reflectance and transmittance from the fitted dielectric constants.

of BTS, respectively. From the measured optical properties, we conclude that the bulk BTS is plasmonic at the 633 nm wavelength, and the plasmon wavelength is on the order of the incident wavelength as expected for bulk materials. However, at the infrared wavelength of $10.6~\mu m$, the extracted plasmon wavelength is very short, that is, more than 100 times smaller than the incident wavelength. This is due to the two-dimensional nature of SS, similar to that observed in graphene. The strong optical confinement of the surface state plasmons can be exploited for various applications including integrated optical circuits and subwavelength optical devices.

■ RESULTS AND DISCUSSION

Our BTS crystals are synthesized by the Bridgman technique and the topological nature of crystal is verified by ARPES measurement.²³ BTS flakes are prepared by tape exfoliation from the bulk and are characterized by Raman spectroscopy as shown in Supporting Information (SI) Figure S1. We first investigated the optical properties of BTS flakes by reflection and transmission measurements. For the wavelengths from 480 to 1600 nm, optical measurements are performed using a

home-built system with BTS exfoliated on calcium fluoride (CaF₂) substrate. For wavelengths from 2.5 to 11 μ m, an undoped Si substrate is used and measurements are performed using Fourier-transform infrared spectroscopy (FTIR) as CaF₂ is opaque beyond \sim 9 μ m. Reflection and transmission measurements are performed on a 15 nm thick flake at visible wavelengths and on a 55 nm thick flake at infrared wavelengths. A thicker (and larger) film is used for IR measurements because the spot size of the IR beam is larger, which requires a larger flake. The optical measurements were then used to obtain optical properties of the surface layer and bulk BTS. We modeled BTS as a three-layer material, that is, surface layer, bulk, and surface layer. The surface layer is modeled as a Drude layer and the bulk is modeled using a Tauc-Lorentz model as in other topological materials. 12 Kramers-Kronig relation is used in the Tauc-Lorentz model. The best-fit parameters of the Drude and Tauc-Lorentz model are shown in SI Note 2. The dielectric constants of bulk BTS and surface layer obtained by the three-layer model are shown in Figure 1a. The dielectric constants of bulk BTS until 1.6 µm are shown in Figure 1b. Negative permittivity is observed below 650 nm. This bulk plasmonic response is

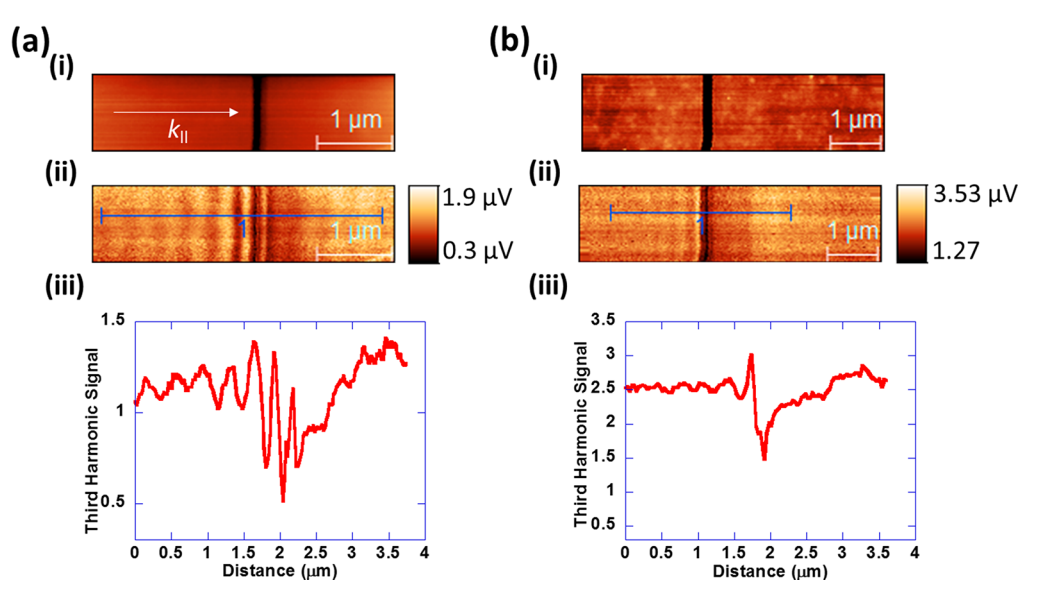


Figure 3. Near-field amplitude image at 633 nm obtained using scattering NSOM. (i) AFM topography, (ii) NSOM amplitude, and (iii) amplitude profile of the blue line in panel ii, for different BTS flakes. (a) Seventy-seven nanometers thick and (b) 15 nm thick.

attributed to the interband absorption dispersion and is not from the bulk free carriers as reported for BSTS. ¹² From the dielectric constants shown in Figure 1a, we see that there are two peaks in ϵ_2 of bulk at ~800 nm and ~2.5 μ m. These two peaks are in reasonable agreement with DFT calculations where the first peak in the visible region is attributed to the interband transition near the Γ point in the momentum space and the other peak is due to the transition around the (0.33, -0.5, -0.5) point. ²⁴

We used the same optical properties for both 15 and 55 nm thick flakes, and the reflectance and transmittance from the fitted dielectric constants along with the experimental results are shown in Figure 2. Figure 2a,b shows the reflectance and transmittance data of the 15 nm thick flake at visible wavelengths and Figure 2c,d shows the reflectance and transmittance data of the 55 nm thick flake at infrared wavelengths. The absorption (1–reflectance–transmittance) of the 55 nm flake obtained from FTIR is shown in SI Figure S2. We can clearly see the band edge of BTS at \sim 5 μ m and the slight absorption at energies below the band gap of BTS is due to the surface layers.

To verify the plasmonic behavior of bulk BTS, we use scattering NSOM to image the surface plasmons launched by a nanoscale slit in BTS flake. BTS flakes are exfoliated onto a ${\rm SiO_2/Si}$ substrate and slits are fabricated using focused ion beam milling. NSOM measurements are carried out using a commercial instrument (Neaspec GmbH) capable of operating at a wavelength of 633 nm and 10.6 μ m. Pseudoheterodyne interferometric detection at the third harmonic of tip oscillation frequency is used to obtain the near-field signals.

The sample is first illuminated with a 633 nm laser, at an oblique angle with TM polarization. This will reveal the bulk plasmon behavior as will be seen later. The in-plane component of incident light is perpendicular to the slit as shown in Figure 3a(i). The near-field amplitude from NSOM measurements for two BTS flakes, 77 nm thick (slit width 240 nm) and 15 nm thick (slit width 230 nm), is shown in Figure 3a,b, respectively. Panel (i) shows AFM topography and panel (ii) shows the near-field amplitude. The near-field amplitude at

the slit on another 63 nm thick flake is shown in SI Figure S3a). These measurements are performed using a silicon tip.

The line profile of the near-field amplitude across the blue line in Figure 3a,b(ii) is shown in Figure 3a,b(iii). We observe the interference fringes parallel to the slit on the left side of the slit (side from which light is incident). These fringes are a result of interference between the surface plasmons from bulk BTS (Real(ε) < 0, Figure 1), launched at the slit, and the inplane component of the incident light. The TM polarized light can launch surface plasmon polaritons on both sides of a slit, which propagate away from the slit. These surface plasmons interfere with the incident field, forming fringes on both sides of the slit. Because of the different propagation directions of the surface plasmons with respect to the incident field, the interference fringe periods are different on the two sides of the slit and can be described as 25,26

$$\Lambda^{-} = \frac{\lambda_0 \lambda_{SP}}{(\lambda_0 + \lambda_{SP} \sin(\theta) \cos(\varphi))}$$
(1)

$$\Lambda^{+} = \frac{\lambda_{0}\lambda_{SP}}{(\lambda_{0} - \lambda_{SP}\sin(\theta)\cos(\varphi))}$$
 (2)

where Λ^- is the fringe period on the incident light side, Λ^+ is the fringe period on the other side, λ_0 is the wavelength of the incident light, λ_{SP} is the wavelength of the surface plasmons, θ is the angle of incidence with respect to the surface normal (oblique angle of 47° in our experiments), and φ is the complementary angle between the in-plane component of incident light and the slit (angle of 0° as in the case of experiments in Figure 3). The λ_{SP} at the interface of dielectric (ε_1) and metal (ε_2) is given as (ε_1)

$$\lambda_{\rm SP} = \frac{\lambda_0}{\text{Real}\left(\sqrt{\frac{\varepsilon_1 \varepsilon_2}{\varepsilon_1 + \varepsilon_2}}\right)} \tag{3}$$

Considering air, $\varepsilon_1 = 1$, and bulk BTS, $\varepsilon_2 = -1.55 + i33.06$ (from Figure 1) at the incident wavelength of 633 nm, the periods Λ^- and Λ^+ estimated from eqs 1 and 2 are 365 nm and 2.35 μ m, respectively. From Figure 3, we observe the

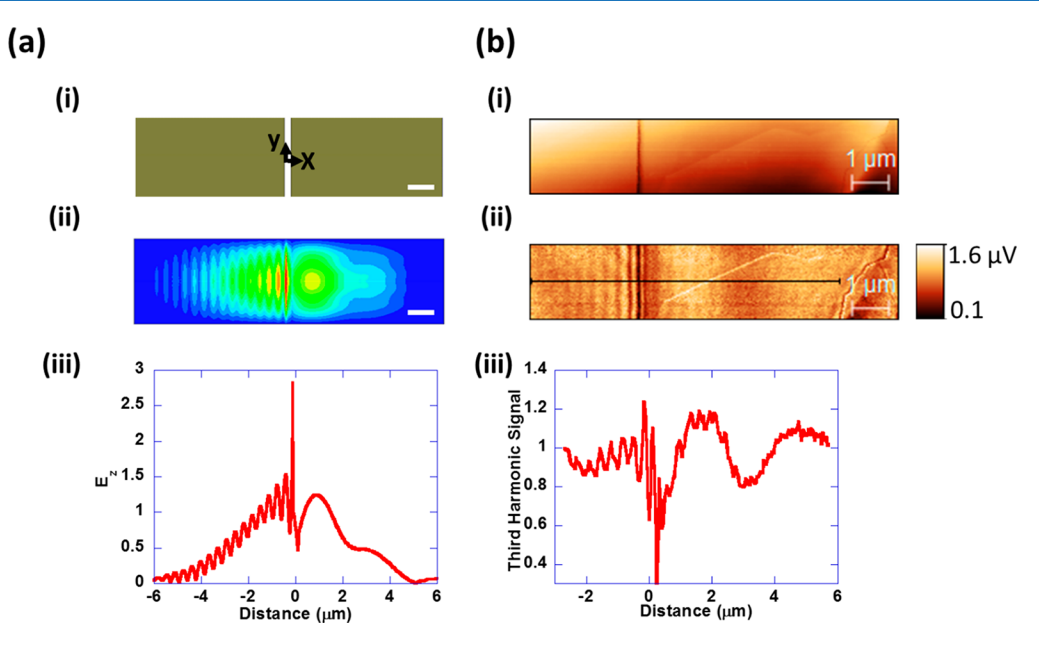


Figure 4. Comparison of the numerical and experimental results at 633 nm. (a) Numerical calculation of a Gaussian beam of radius 2 μ m radiating on the nanoslit. Scale bar is 1 μ m. (i) Geometry of the simulation showing the slit. (ii) Electric field distribution on a plane, 2 nm above surface. (iii) Line profile of E_z at the center of the plane (along the x-axis) 2 nm above the surface. (b) Near-field amplitude image at 633 nm using scattering-type NSOM (i), AFM topography (ii), and s-NSOM amplitude (iii). Amplitude profile of the black line in panel b(ii).

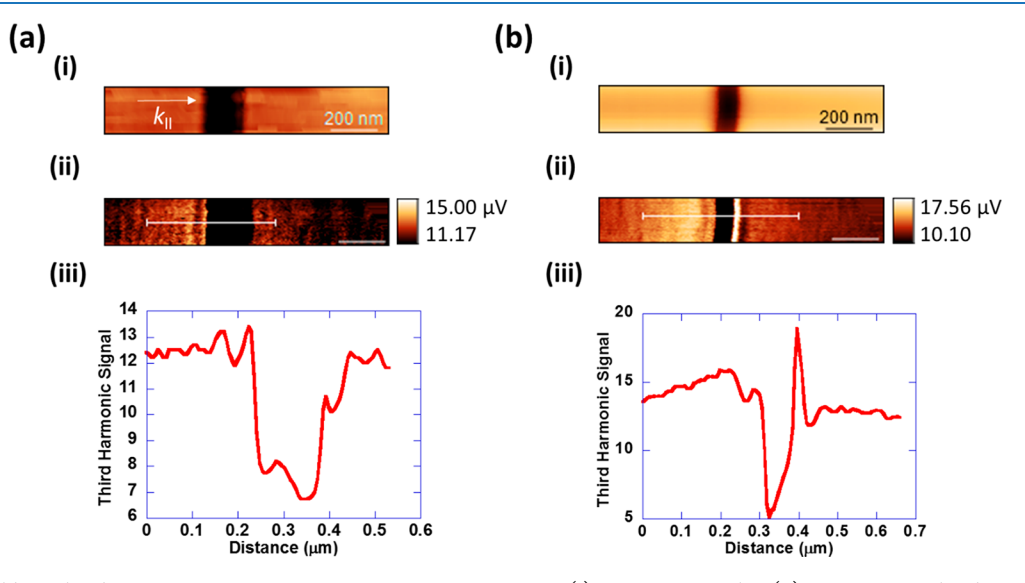


Figure 5. Near-field amplitude image at $10.6 \, \mu m$ using scattering-type NSOM. (i) AFM topography, (ii) s-NSOM amplitude, and (iii) amplitude profile of the white line in panel ii, for different BTS flakes. (a) Fifteen nanometers thick and (b) 77 nm thick. All scale bars are 200 nm.

interference fringes to the left side of the slit but no fringe to the right of the slit due to the finite scan window. (A large scan is shown later in Figure 4b). The experimental fringe spacing to the left of the slit of 15, 63, and 77 nm thick flakes are 315, 364, and 301 nm, which are in close agreement to the estimated fringe spacing. Hence, the observed interference fringes can indeed be attributed to the interference of surface plasmons from the bulk BTS and the incident beam.

To further illustrate the formation of fringes, numerical calculations are performed using ANSYS EM (see Methods). The simulation model consists of a 77 nm BTS film on top of a SiO_2/Si substrate with a 240 nm wide slit as in the experiment. The results of the electric field at 2 nm above the BTS surface is shown in Figure 4a(ii). As NSOM is more sensitive to the vertical component of the electric field, ²⁷ the simulation result

of the electric field component E_z , on a line along the x-axis (see Figure 4a(i)) is shown in Figure 4a(iii). We clearly see the fringes on the left side of the slit and the intensity variation on the right. The simulated fringe spacing to the left of the slit is 359 nm. However, the fringe spacing of 2.35 μ m on the right side of the slit cannot be observed precisely due to the limited size of the Gaussian beam (radius = 2 μ m). The experimental results of a large area scan is shown in the Figure 4b. The experimental fringe spacing to the left of the slit is 360 nm, and is over 2 μ m on the right side, in agreement with numerical calculations

From the analytical model, the fringe period on the left side of the slit, Λ^- , increases with φ . To verify the dependence of interference fringes on φ , we did near-field measurements with different slit orientations (φ) with respect to the in-plane

component of the incident light, and the results are shown in SI Figure S4. We observe that the fringe spacing increases with φ , in a reasonable agreement with the analytical model.

In addition, we performed near-field measurements with an incident wavelength of 532 nm. We observed fringes toward the incident light side, similar to the results at 633 nm wavelength. The experimental fringe spacing is ~300 nm and the fringe spacing Λ^- calculated from eq 1 is 292 nm (θ = 58°, φ = 16° as in the experiment). Therefore, the measured fringe space is in good agreement with the fringe space determined analytically. The fringe spacing at 532 nm is less than that from 633 nm as they are determined by the incident wavelength and the plasmon wavelength which in turn is determined by the dielectric constants (eq 1).

It is known that AFM tip can also launch surface plasmons.²⁸ Interference patterns were observed in graphene at infrared wavelength and interpreted as the interference of surface plasmons launched by the AFM tip and its reflection at the boundary.^{10,11} In our experiments, different fringe spacing on either side of the slit and the variation of fringe spacing at different slit orientations cannot be explained by surface plasmons launched by the tip. For tip-launched plasmons, the fringe spacing would be the same on either side, and the spacing is invariant with the slit orientation. Hence, in our case the observed fringes are formed by the interference of surface plasmons launched at the slit and the incident field, with minimal effect from the tip.

To study the plasmons of the surface state, the sample is illuminated with a below bulk band gap energy, 10.6 µm wavelength laser, at an oblique angle with TM polarization. The Pt tip is used for the infrared measurements to increase the signal. The band gap of the bulk BTS from our measurements and literature²⁹ is ~0.24 eV. With a below band gap excitation energy of 0.116 eV (10.6 μ m wavelength), there will be no contribution from the bulk. The in-plane component of the incident light is perpendicular to the slit as shown in Figure 5a(i). The near-field amplitudes from NSOM measurements for two BTS flakes 15 and 77 nm thick are shown in Figure 5a,b, respectively. The near-field amplitude at the slit on another 63 nm thick flake is shown in SI Figure S3(b). The line profile of the near-field amplitude is shown in Figure 5(iii). We observe a fringe spacing of ~49 nm on the left side of the slit and ~55 nm on the right side of the slit for the 15 nm thick flake, ~36 nm on the left side of the slit and ~50 nm on the right side of the slit for the 63 nm thick flake, and ~51 nm on the right side of the slit for the 77 nm thick flake. (The fringe spacing on the left side of the slit for 77 nm flake cannot be determined precisely.) Hence, the observed fringe spacing is ~50 nm, much smaller than the incident wavelength $\sim (\lambda/200)$. We note that the near-field signal is weak and to confirm the fringes, line scans at different locations and Fourier transform of the line scan of 15 nm flake and 77 nm flake are performed and are shown in SI Note 6.

The smaller fringe spacing is attributed to the plasmons from the surface state of topological insulator. Small fringe spacing of plasmons were reported for graphene, ${\sim}100$ nm (with 11.2 μm incident wavelength) and ${\sim}130$ nm (with 9.7 μm incident wavelength). These small fringe spacings in graphene were explained with the theory of plasmons in two-dimensional metal. The origin of fringes was interpreted as the interference of the plasmons launched by the AFM tip and its reflection from the boundary of the graphene with a fringe spacing of half the plasmon wavelength. Another study also

confirmed tip-excited plasmons in graphene with 10.6 μ m excitation wavelength. One of the features in tip-excited plasmon is that the fringe spacing is half of the plasmon wavelength. Here, we also interpret our fringes as the interference between tip launched plasmons and its reflection. Hence, the plasmon wavelength of surface state excited by 10.6 μ m wavelength is ~100 nm (from the fringe spacing of ~50 nm), similar to that in graphene.

To illustrate further, the surface plasmons arising from the surface state of the topological insulator is analyzed as Dirac plasmons from 2D electrons. ¹² In thin films, surface electrons at the interfaces of topological insulator—vacuum and topological insulator—substrate interact via an effective Coulomb potential. ³¹ This interaction produces two plasmon modes, optical and acoustic plasmon modes. ^{15,31,32} The dispersion of the acoustic mode depends on the permittivity of the topological insulator bulk and is strongly Landau-damped (i.e., not observable). ¹⁵ The dispersion of the optical mode depends on the permittivity of the outer dielectric media (air and substrate in our case) ^{31,32} and is given by the following expression ¹⁵

$$\nu(k) = \frac{1}{2\pi} \sqrt{k} \left(\frac{e^2}{4\pi\varepsilon_o \varepsilon \left(\frac{h}{2\pi}\right)} v_f \sqrt{2\pi n_d} \right)^{1/2}$$
(4)

where ε is the averaged dielectric constants of the air and substrate, $v_{\rm f}$ is the Fermi velocity, $n_{\rm d}$ is the carrier density, ν is the frequency of the light, e is the electronic charge, and $\varepsilon_{\rm o}$ is the permittivity of free space. In our BTS, with a Fermi velocity of 6×10^5 m/s and SS carrier concentration of $n_{\rm d} \sim 10^{13}$ cm⁻², 33,34 we obtain an SS plasma wavelength of $\lambda_{\rm p} = 2\pi/k$ as 74 nm, slightly smaller than the average measured value which can be due to various factors such as variation in the carrier concentration and accuracy in the fringe spacing measurements.

The studies above show that BTS exhibit plasmonic behavior across a wide wavelength range. The plasmonic response in mid-IR arises from SS and is dominated by bulk in vis-UV wavelengths. The short wavelength of SS plasmons in

mid-IR with a ratio $\left(\frac{\lambda_{IR}}{\lambda_p}\right)$ of 106 (λ_{IR} is the incident wavelength and λ_p is the plasmon wavelength) is observed, much higher that of the metals. The plasmonic behavior at mid-IR wavelengths can open up various applications including thermal radiation control, surface-enhanced spectroscopy, 35 that all the plasmonic desired plasmonic plants and the second plasmonic plants and plasmonic plants are the second plants.

thermal radiation control, surface-enhanced spectroscopy,³⁵ and broadband plasmonic devices. Plasmonic switching and active control of the SS plasmons by electrical gating as in graphene^{10,11} should also be possible. In addition, spin-polarized SS provide exciting opportunities for plasmon-spintronic devices controllable by external EM or magnetic fields.³⁶

CONCLUSIONS

In summary, we studied the surface plasmons arising from bulk and SS of BTS. Surface plasmons arising from bulk are studied using the incident wavelength of 633 nm and surface plasmons from SS are studied with a below band gap excitation of 10.6 μ m. The plasmon wavelength of the bulk is on the order of incident light wavelength, in sharp contrast to the very short SS plasmon wavelength, that is, more than 100 times smaller than the incident light wavelength. The short SS plasmon

wavelength is due to the two-dimensional nature of SS, similar to the plasmon behavior in graphene. The strong optical confinement of the surface state plasmons can be exploited for various applications including integrated optical circuits and subwavelength optical devices.

METHODS

Sample Preparation. BTS flakes are exfoliated from bulk using scotch tape. For optical measurements in the wavelength range from 480 to 1600 nm, flakes are exfoliated onto CaF_2 substrate; in the range from 2.5 to 11 μ m, flakes are exfoliated onto an undoped Si substrate for both transmission and reflection measurements. For near-field measurements, flakes are exfoliated onto SiO_2/Si substrate. The thickness of oxide is 270 nm. Slits in BTS are fabricated using focused ion beam milling.

Optical Measurements. Reflection and transmission measurements in the wavelength range from 480 to 1600 nm are measured using a home-built system. The light source is a quartz tungsten halogen lamp and spectrometers (UV–vis Ocean Optics and Princeton instruments Acton SP2300) are used to obtain the spectral information. Optical measurements in the range from 2.5 to 11 μ m are performed using commercial Fourier-transform infrared spectroscopy (Thermo Nicolet Nexus 670 FTIR).

Modeling of Optical Constants. The optical measurements are fitted to obtain the optical properties of the surface layer and bulk BTS using Fresnel equations. We modeled BTS as a three-layer material, that is, surface layer, bulk, and surface layer. The surface layer is modeled as a Drude layer and the bulk by using a Tauc—Lorentz model. MATLAB code for Fresnel equations in a multilayer structure is used to obtain the optical constants. The top and bottom surface layer are modeled with the same dielectric constants. Details of the model are given in SI Note 2.

Near-Field Measurements. Near-field measurements are carried out using a commercial scattering-type NSOM system (Neaspec GmbH) equipped with a visible laser of 633 nm wavelength and an infrared laser of 10.6 µm. The NSOM system is based on an AFM system of tapping mode: a sharp AFM tip (typically with a curvature radius about 20 nm) was approached to the surface of the sample and vibrated vertically with a 50 nm amplitude at a frequency around 260 kHz. TM polarized light of either 633 nm or 10.6 µm wavelength was focused and incident via a parabolic mirror onto both the tip and sample at an angle of 47° to the surface normal. The tipscattered light was then recorded by a pseudoheterodyne interferometer. In order to suppress background scattering, the detected signal was demodulated at higher harmonic frequencies (in this work the third harmonic is used for all the images). Pt tip is used for the infrared measurements where as both Si and Pt tips are used for 633 nm measurements. The 633 nm measurements shown in the main text are performed using Si tip.

Numerical Simulations. Numerical calculations are performed using the finite element electromagnetic solver, ANSYS EM 17.1 with radiation boundary conditions. The geometry consists of air, BTS, and $\mathrm{SiO}_2/\mathrm{Si}$ substrate. BTS is modeled as three-layer material with optical properties of bulk and surface layer from the fitted optical constants. Light is illuminated from air side with an oblique incident angle of 47° and TM polarization. A Gaussian beam with radius of 2 μ m is focused at the center of the slit.

ASSOCIATED CONTENT

Supporting Information

The Supporting Information is available free of charge on the ACS Publications website at DOI: 10.1021/acsphotonics.9b00814.

Characterization of BTS flakes by Raman spectroscopy, Tauc-Lorentz and Drude model for BTS, band edge of BTS flake, near-field measurements of a 63 nm thick flake, near-field measurements with different slit orientations, and line scans of near-field signal at 10.6 μ m wavelength (PDF)

AUTHOR INFORMATION

Corresponding Author

*E-mail: xxu@ecn.purdue.edu.

ORCID ®

Xianfan Xu: 0000-0003-0580-4625

Author Contributions

X.X. conceived the idea, designed, and supervised the experiments and numerical analyses. P.V. prepared the samples and led the optical measurements and numerical simulations. P.V. modeled the optical constants and analyzed the near-field measurements. X.W. performed the near-field measurements. V.I. built the optical setup for visible and near IR wavelengths and helped in optical measurements. Y.C. provided the material and helped in the discussion. All authors cowrote the manuscript.

Notes

The authors declare no competing financial interest.

ACKNOWLEDGMENTS

Funding provided by the National Science Foundation (EFMA-1641101) is gratefully acknowledged. The authors would like to thank the Center for Micro- and Nanoscale Research and Fabrication of the University of Science and Technology of China for the sample characterization and Dr. Ireneusz Miotkowski for synthesizing the BTS crystals.

REFERENCES

- (1) Maier, S. A.; Kik, P. G.; Atwater, H. A.; Meltzer, S.; Harel, E.; Koel, B. E.; Requicha, A. A. G. Local Detection of Electromagnetic Energy Transport below the Diffraction Limit in Metal Nanoparticle Plasmon Waveguides. *Nat. Mater.* **2003**, *2*, 229–232.
- (2) Fang, Y.; Sun, M. Nanoplasmonic Waveguides: Towards Applications in Integrated Nanophotonic Circuits. *Light: Sci. Appl.* **2015**, *4*, e294.
- (3) Rodrigo, D.; Limaj, O.; Janner, D.; Etezadi, D.; Garcia de Abajo, F. J.; Pruneri, V.; Altug, H. Mid-Infrared Plasmonic Biosensing with Graphene. *Science* **2015**, 349, 165–168.
- (4) Punj, D.; Mivelle, M.; Moparthi, S. B.; Van Zanten, T. S.; Rigneault, H.; Van Hulst, N. F.; García-Parajó, M. F.; Wenger, J. A Plasmonic "antenna-in-Box" Platform for Enhanced Single-Molecule Analysis at Micromolar Concentrations. *Nat. Nanotechnol.* **2013**, *8*, 512–516
- (5) De Angelis, F.; Patrini, M.; Das, G.; Maksymov, I.; Galli, M.; Businaro, L.; Andreani, L. C.; Di Fabrizio, E. A Hybrid Plasmonic-Photonic Nanodevice for Label-Free Detection of a Few Molecules. *Nano Lett.* **2008**, *8*, 2321–2327.
- (6) Atwater, H. A.; Polman, A. Plasmonics for Improved Photovoltaic Devices. *Nat. Mater.* **2010**, *9*, 205–213.
- (7) Venuthurumilli, P. K.; Ye, P. D.; Xu, X. Plasmonic Resonance Enhanced Polarization-Sensitive Photodetection by Black Phosphorus in Near Infrared. *ACS Nano* **2018**, *12*, 4861–4867.

(8) Liu, Y.; Cheng, R.; Liao, L.; Zhou, H.; Bai, J.; Liu, G.; Liu, L.; Huang, Y.; Duan, X. Plasmon Resonance Enhanced Multicolour Photodetection by Graphene. *Nat. Commun.* **2011**, *2*, 579.

- (9) Naik, G. V.; Shalaev, V. M.; Boltasseva, A. Alternative Plasmonic Materials: Beyond Gold and Silver. *Adv. Mater.* **2013**, *25*, 3264–3294.
- (10) Fei, Z.; Rodin, A. S.; Andreev, G. O.; Bao, W.; McLeod, A. S.; Wagner, M.; Zhang, L. M.; Zhao, Z.; Thiemens, M.; Dominguez, G.; Fogler, M. M.; Neto, A. H. C.; Lau, C. N.; Keilmann, F.; Basov, D. N. Gate-Tuning of Graphene Plasmons Revealed by Infrared Nano-Imaging. *Nature* **2012**, *487*, 82–85.
- (11) Chen, J.; Badioli, M.; Alonso-González, P.; Thongrattanasiri, S.; Huth, F.; Osmond, J.; Spasenović, M.; Centeno, A.; Pesquera, A.; Godignon, P.; Elorza, A. Z.; Camara, N.; Abajo, F. J. G.; Hillenbrand, R.; Koppens, F. H. L. F. Optical Nano-Imaging of Gate-Tunable Graphene Plasmons. *Nature* **2012**, *487*, 77–81.
- (12) Ou, J. Y.; So, J. K.; Adamo, G.; Sulaev, A.; Wang, L.; Zheludev, N. I. Ultraviolet and Visible Range Plasmonics in the Topological Insulator Bi1.5Sb0.5Te1.8Se1.2. *Nat. Commun.* **2014**, *5*, 5139.
- (13) Fu, L.; Kane, C. L. Topological Insulators with Inversion Symmetry. *Phys. Rev. B: Condens. Matter Mater. Phys.* **2007**, *76*, 045302.
- (14) Roushan, P.; Seo, J.; Parker, C. V.; Hor, Y. S.; Hsieh, D.; Qian, D.; Richardella, A.; Hasan, M. Z.; Cava, R. J.; Yazdani, A. Topological Surface States Protected from Backscattering by Chiral Spin Texture. *Nature* **2009**, *460*, 1106–1109.
- (15) Di Pietro, P.; Ortolani, M.; Limaj, O.; Di Gaspare, A.; Giliberti, V.; Giorgianni, F.; Brahlek, M.; Bansal, N.; Koirala, N.; Oh, S.; Calvani, P.; Lupi, S. Observation of Dirac Plasmons in a Topological Insulator. *Nat. Nanotechnol.* **2013**, *8*, 556–560.
- (16) Zhao, M.; Bosman, M.; Danesh, M.; Zeng, M.; Song, P.; Darma, Y.; Rusydi, A.; Lin, H.; Qiu, C.-W.; Loh, K. P. Visible Surface Plasmon Modes in Single Bi2Te3 Nanoplate. *Nano Lett.* **2015**, *15*, 8331–8335.
- (17) Dubrovkin, A. M.; Adamo, G.; Yin, J.; Wang, L.; Soci, C.; Wang, Q. J.; Zheludev, N. I. Visible Range Plasmonic Modes on Topological Insulator Nanostructures. *Adv. Opt. Mater.* **2017**, *5*, 1600768.
- (18) Yuan, J.; Ma, W.; Zhang, L.; Lu, Y.; Zhao, M.; Guo, H.; Zhao, J.; Yu, W.; Zhang, Y.; Zhang, K.; Hoh, H. Y.; Li, X.; Loh, K. P.; Li, S.; Qiu, C. W.; Bao, Q. Infrared Nanoimaging Reveals the Surface Metallic Plasmons in Topological Insulator. *ACS Photonics* **2017**, *4*, 3055–3062.
- (19) Ren, Z.; Taskin, A. A.; Sasaki, S.; Segawa, K.; Ando, Y. Large Bulk Resistivity and Surface Quantum Oscillations in the Topological Insulator Bi2Te2Se. *Phys. Rev. B: Condens. Matter Mater. Phys.* **2010**, 82, 241306
- (20) Xiong, J.; Luo, Y.; Khoo, Y.; Jia, S.; Cava, R. J.; Ong, N. P. High-Field Shubnikov-de Haas Oscillations in the Topological Insulator Bi2Te2Se. *Phys. Rev. B: Condens. Matter Mater. Phys.* **2012**, *86*, 45314.
- (21) Maier, S. A. Plasmonics: Fundamentals and Applications; Springer: New York, 2007.
- (22) Gramotnev, D. K.; Bozhevolnyi, S. I. Plasmonics beyond the Diffraction Limit. *Nat. Photonics* **2010**, *4*, 83–91.
- (23) Cao, H.; Liu, C.; Tian, J.; Xu, Y.; Miotkowski, I.; Hasan, M. Z.; Chen, Y. P. Controlling and Distinguishing Electronic Transport of Topological and Trivial Surface States in a Topological Insulator. arXiv:1409.3217 2014.
- (24) Yin, J.; Krishnamoorthy, H. N.; Adamo, G.; Dubrovkin, A. M.; Chong, Y.; Zheludev, N. I.; Soci, C. Plasmonics of Topological Insulators at Optical Frequencies. *NPG Asia Mater.* **2017**, *9*, e425.
- (25) Wang, B.; Aigouy, L.; Bourhis, E.; Gierak, J.; Hugonin, J. P.; Lalanne, P. Efficient Generation of Surface Plasmon by Single-Nanoslit Illumination under Highly Oblique Incidence. *Appl. Phys. Lett.* **2009**, *94*, 011114.
- (26) Li, Y.; Zhou, N.; Kinzel, E. C.; Ren, X.; Xu, X. The Origin of Interferometric Effect Involving Surface Plasmon Polariton in Scattering Near-Field Scanning Optical Microscopy. *Opt. Express* **2014**, 22, 2965.

- (27) Lee, K. G.; Kihm, H. W.; Ahn, K. J.; Ahn, J. S.; Suh, Y. D.; Lienau, C.; Kim, D. S. Vector Field Mapping of Local Polarization Using Gold Nanoparticle Functionalized Tips: Independence of the Tip Shape. *Opt. Express* **2007**, *15*, 14993.
- (28) Krug, J. T.; Sánchez, E. J.; Xie, X. S. Design of Near-Field Optical Probes with Optimal Field Enhancement by Finite Difference Time Domain Electromagnetic Simulation. *J. Chem. Phys.* **2002**, *116*, 10895
- (29) Akrap, A.; Tran, M.; Ubaldini, A.; Teyssier, J.; Giannini, E.; Van Der Marel, D.; Lerch, P.; Homes, C. C. Optical Properties of Bi2Te2Se at Ambient and High Pressures. *Phys. Rev. B: Condens. Matter Mater. Phys.* **2012**, *86*, 235207.
- (30) Cheng, G.; Wang, D.; Dai, S.; Fan, X.; Wu, F.; Li, X.; Zeng, C. Nano-Imaging of an Edge-Excited Plasmon Mode in Graphene. *Nanoscale* **2018**, *10*, 16314–16320.
- (31) Profumo, R. E. V; Asgari, R.; Polini, M.; Macdonald, A. H. Double-Layer Graphene and Topological Insulator Thin-Film Plasmons. *Phys. Rev. B: Condens. Matter Mater. Phys.* **2012**, 85, 85443.
- (32) Stauber, T. Plasmonics in Dirac Systems: From Graphene to Topological Insulators. *J. Phys.: Condens. Matter* **2014**, 26, 123201.
- (33) Luo, Z.; Tian, J.; Huang, S.; Srinivasan, M.; Maassen, J.; Chen, Y. P.; Xu, X. Large Enhancement of Thermal Conductivity and Lorenz Number in Topological Insulator Thin Films. *ACS Nano* **2018**, *12*, 1120–1127.
- (34) Iyer, V.; Chen, Y. P.; Xu, X. Ultrafast Surface State Spin-Carrier Dynamics in the Topological Insulator Bi2Te2Se. *Phys. Rev. Lett.* **2018**, *121*, 026807.
- (35) Neubrech, F.; Pucci, A.; Cornelius, T. W.; Karim, S.; García-Etxarri, A.; Aizpurua, J. Resonant Plasmonic and Vibrational Coupling in a Tailored Nanoantenna for Infrared Detection. *Phys. Rev. Lett.* **2008**, *101*, 157403.
- (36) Appelbaum, I.; Drew, H. D.; Fuhrer, M. S. Proposal for a Topological Plasmon Spin Rectifier. *Appl. Phys. Lett.* **2011**, 98, 023103.